

GRAIN-SCALE DEFORMATION MECHANISMS IN AN ADDITIVELY MANUFACTURED ALUMINIUM BRONZE OLIGOCRYSTAL

**Varvara Romanova¹, Dmitry Lychagin², Maxim Pisarev¹,
Olga Zinovieva³, Ruslan Balokhonov¹**

¹Institute of Strength Physics and Materials Science, Tomsk, Russia

²National Research Tomsk State University, Tomsk, Russia

³School of Engineering and Technology,
University of New South Wales Canberra, ACT, Australia

Abstract. *Oligocrystals provide a unique material for in-depth analysis of deformation mechanisms in metals and alloys. In this paper, the deformation mechanisms in a Cu-7.5 wt.% Al oligocrystal are investigated experimentally and numerically. An experimental sample containing several coarse columnar grains is produced by wire-feed electron-beam additive manufacturing. Based on the experimental data, a crystal plasticity finite element model is built to consider realistic grain shape and orientations. This study involves a comprehensive analysis of experimental data, numerical results and analytical estimates to reveal the peculiarities of slip activation in oligocrystal grains under compression. Experimental and numerical findings have shown that along with slip systems with the highest Schmid factors, other slip systems are activated in most grains to accommodate their plastic deformation. To elucidate why the slip systems with non-maximal Schmid factors became active, we examined the stress fields within the grains. It was revealed that the stress state at the grain scale deviated from uniaxial. Finally, a detailed numerical analysis of strain rate dynamics demonstrated that plastic deformation in particular grains developed in the form of narrow fronts. These fronts periodically generated near the moving punch and subsequently propagated towards the opposite side of the sample. The study has shown that oligocrystal analysis provides valuable insights into the linkage between the intra- and intergrain deformation mechanisms with the overall material behaviour.*

Key words: *Additive Manufacturing, Directed Energy Deposition, Oligocrystals, Crystal Plasticity, Slip Systems, Microstructure-Based Mechanical Simulation*

Received: November 28, 2023 / Accepted January 11, 2024

Corresponding author: Varvara Romanova

Institute of Strength Physics and Materials Science SB RAS, Akademicheskii prospect 2/4, 634055 Tomsk, Russia

E-mail: varvara@ispms.tsc.ru

1. INTRODUCTION

Advanced tribology puts into play a wide range of challenging problems requiring the joint efforts of experts in physics, mechanics, and materials science. Among the key issues is the prediction of the deformation and fracture behaviour under an external load applied to the material surface. Classical contact mechanics focuses on the macroscopic quantities relating the stress and strain distributions in a subsurface layer with the parameters of an external load applied to the contact surface [1–3]. While valuable, this approach commonly neglects lower-scale deformation mechanisms which are first to occur in a loaded material. Meanwhile, understanding the multiscale deformation mechanisms is crucial in view of fracture prediction since progressive damage accumulation at lower scales is a precursor of larger-scale deformation and fracture [4].

Oligocrystals (sometimes called oligocrystals) represent a unique material for the detailed study of deformation mechanisms in metals and alloys throughout length scales. Oligocrystals contain several millimetre-sized columnar grains with known orientations that span through the sample thickness [5, 6]. Due to the limited number of grains in a sample, the complexity of factors influencing deformation mechanisms is significantly reduced. This reduction facilitates the detailed analysis of the microstructural effects on the deformation process and mechanical properties of a material. The investigation of oligocrystals thus offers a more controlled and insightful approach to understanding deformation mechanisms in materials.

Despite the significant potential of oligocrystals for fundamental research, a limited number of oligocrystal deformation studies are reported in the literature [7]. The authors [7,8] considered oligocrystal research as an excellent opportunity for the development of advanced experimental characterisation techniques. Several research groups focused on the experimental grain-scale validation of the implemented crystal plasticity models considering oligocrystals [9–12], which is particularly interesting given the extremes of oligocrystals with the microstructural and macrostructural spatial scales being of the same order of magnitude.

Playing a key role in tribological applications, deformation-induced surface roughening represents another important research topic. Being an intrinsic phenomenon, multiscale surface asperities evolving in plastic deformation are considered as the evidence of deformation mechanisms acting at different spatial scales [13]. In single crystals, alterations in the surface morphology typically appear as multiple slip bands and, at a lower scale, slip steps created by dislocations leaving the bulk [14,15]. In polycrystals, at different spatial scales surface roughening becomes evident as microscale slip steps, grain scale orange peel phenomenon caused by out-of-plane displacement of individual crystals, mesoscale ridging and roping induced by collective deformation of groups of grains, and macroscopic waviness at the specimen length scale [13,16]. Few researchers have analysed surface roughening in oligocrystals [9,11,17].

Additive manufacturing (AM) has opened up groundbreaking opportunities for fabricating oligocrystals [18]. An advantageous 3D printing technology for manufacturing large metal parts is wire-feed electron beam directed energy deposition AM (DED-EB type of AM technology; this work will use the abbreviation WEB-AM following [19–22]). WEB-AM utilises a power electron beam to melt metal wire feedstock as it is deposited through a feeder track-by-track and layer-by-layer. Typically for WEB-AM, coarse

columnar grains grow throughout multiple layers up to several millimetres in length due to directional solidification.

Using a combined experimental and computational approach, this paper considers the grain-scale deformation mechanisms in a WEB-AM aluminium bronze oligocrystal in a compression test. Special focus is placed on the analysis of microscale stress and strain fields and their interrelation with the activation of slip systems in surface grains and the evolution of surface morphology. The paper is structured as follows. The experimental procedure of sample fabrication, microstructure characterisation and mechanical testing is detailed in Section 2. Based on the experimental data, a micromechanical crystal plasticity finite element (CPFE) model is constructed in Section 3. Experimental and computational results are presented and discussed in Section 4. The summary of the main findings is given in Conclusion.

2. EXPERIMENTAL METHODS

2.1 Sample Fabrication

A build of $90 \times 20 \times 40$ mm was fabricated from Cu-7.5 wt.% Al wire with a diameter of 1 mm using a wire-feed electron beam directed energy deposition machine (ISPMS SB RAS, Tomsk, Russia). The WEB-AM printing was performed in vacuum with the following parameters: the electron beam accelerating potential – 30 kV; the beam current – 50 mA; the spot size – 4.5 mm; the beam sweep frequency – 1000 Hz; and the heat input – 0.22 kJ/mm. The AISI 321 steel base plate was mounted on the table moving under the gun in a zigzag fashion at 5 mm/s to print a layer with a thickness of 2 mm. The time delay between printing subsequent layers was 2-3s.

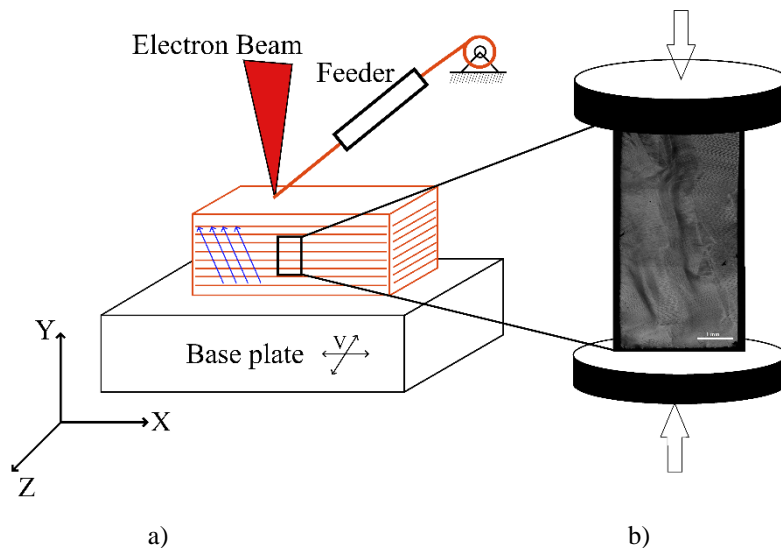


Fig. 1 Schematics of WEB-AM printing (a) and compression test (b)

A sample for compression testing was cut from the middle part of the build in the form of a rectangular bar measuring $3.5 \times 7 \times 3.5$ mm along the X, Y and Z, respectively. Hereinafter, Y is parallel and X and Z are perpendicular to the build direction (BD), where X is considered as the scanning direction. The WEB-AM printing and compression testing are illustrated schematically in Fig. 1a. The sample lateral side perpendicular to the Z-axis was subjected to sandpaper grinding (Mirka) and diamond suspension polishing. The final stage of surface preparation was ion beam milling at 10 kV for 15 min using the SEMPRep2 device (Technoorg Linda Co. Ltd., Budapest, Hungary).

2.2 Microstructure Characterisation

The grain structure on the lateral side of the WEB-AM printed sample (Fig. 1) was analysed by electron backscatter diffraction (EBSD) using a Tescan MIRA 3 LMU scanning electron microscope (TESCAN ORSAY HOLDING, Brno, Czech Republic) equipped with an EBSD detector (Oxford Instruments, High Wycombe, UK). The examined area covered the entire lateral surface with 0.1-0.2 mm margins. The EBSD maps of the grain structure are plotted in Fig. 2 in inverse pole figure (IPF) colours for the X, Y and Z directions. In what follows, grains are referred to by their numbers given in Fig. 2a.

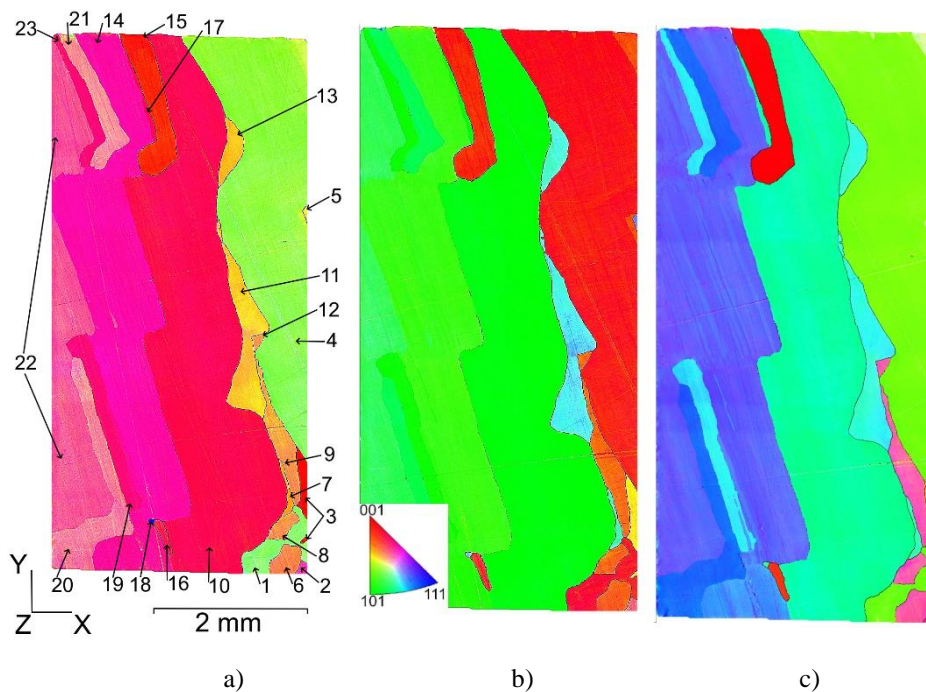


Fig. 2 Orientation maps for WEB-AM aluminium bronze Cu-7.5 wt.% Al in IPF colours for the directions $\parallel Y$ (a), $\parallel Z$ (b) and $\parallel X$ (c)

The analysis of grain misorientation angles revealed that 58% grains are characterised by low angle grain boundaries ($< 15^\circ$), while 42% grains have misorientation angles larger

than 15° . The high angle boundaries are highlighted in the EBSD maps (Fig. 2) to separate 23 individual grains with 16 distinct orientations of crystal lattices.

Several large columnar grains, about 7 mm in length and 1 mm in width, span the entire height of the sample (Grains 4, 10, 14 and 22 in Fig. 2). A set of finer grains appearing near the bottom surface might be the evidence of larger grains located below the surface. Finer grains observed in between the coarse grain boundaries might be the part of larger grains growing in parallel XY planes, before or after the plane analysed. The coarse columnar grains tend to grow along the heat flow and tilt to the Y-axis ($Y\parallel BD$) at an angle controlled by the table velocity with respect to the electron beam (see schematics in Fig. 1a). Typically for WEB-AM, stepwise grain boundary regions were formed due to electron beam transition from layer to layer. The 2 mm distance between the boundary steps corresponds to the layer thickness.

The WEB-AM processing gives rise to specific features of grain formation where a set of fine grains may solidify in narrow regions between the coarse columnar grains. Presumably, the red-coloured grains in the left part of the oligocrystal (Fig. 2a) solidified conjointly, while Grain 4 (green-coloured in Fig. 2a) solidified in a standalone manner. This behaviour enabled some additional grains to nucleate and solidify in between these large columnar crystals. The crystal lattices of the three large Grains 14, 10 and 22 have close to Cube orientations, $\langle 100 \rangle \parallel Y$, with low misorientation angles due to a small amount of crystal lattice rotations about the Z-axis. Grain 4 has a nearly Goss orientation with respect to the compression axis, $\langle 110 \rangle \parallel Y$. Both Cube and Goss orientations are characterised by a set of equally loaded octahedral slip systems, which is well documented for single crystals [12,13,23,24]. However, the EBSD data show that in the grains of oligocrystal no slip systems are exactly equally loaded.

2.3 Compression Test and Surface Examination

The schematic of compression testing is shown in Fig. 1b. Compression was applied along the vertical direction with the long axes of columnar grains tilted at an angle of ≈ 18 degrees about the Y-axis. The compression test was carried out at a constant strain rate $2.4 \cdot 10^{-3} \text{ s}^{-1}$ at room temperature according to ASTM A 370 using an Instron ElektroPuls E100000 universal testing machine (Instron, Norwood, MA, USA). After 5% compressive strain, the sample was taken from the testing machine and its surface was analysed using an Olympus LEXT OLS4100 laser scanning microscope (Olympus Corporation, Tokyo, Japan).

3. MICROSTRUCTURE-BASED CPFEM MODEL

The EBSD map (Fig. 2) was graphically processed to obtain a bitmap image subsequently approximated by a 407×880 voxel mesh. Reconstructing a full 3D grain model from the experimental data is a challenging task calling for expensive and time-consuming experimental procedure (e.g., X-ray diffraction tomography [25,26] or serial sectioning techniques [27,28]). In our simulations, we used a simplified 3D model obtained from the 2D experimental image by translation along the Z direction. In the FE implementation, each voxel was treated as a hexahedral finite element (C3D8R). The 3D FE model of $3.2 \times 7.0 \times 0.5$ mm constructed on a $407 \times 880 \times 64$ mesh is shown in Fig. 3a.

The FE model (Fig. 3a) was imported into ABAQUS/Explicit to solve the boundary-value problem in a dynamic formulation (see [29] for further detail). The finite elements belonging to particular grains were organised into sets and assigned local (crystal) coordinate systems with the axes lying along the [100], [010] and [001] crystal directions. The rotations of crystal frames about the global (sample) coordinate system XYZ were given by a set of Euler angles provided by EBSD data (Fig. 2) to fully replicate the experimental data.

The grain behaviour was described in terms of a crystal plasticity model relating the stress and strain tensor components with the dislocation slip in the face-centred cubic (FCC) crystal lattice. Let us dwell briefly on some major points of the model formulation, with the details given at length elsewhere [29].

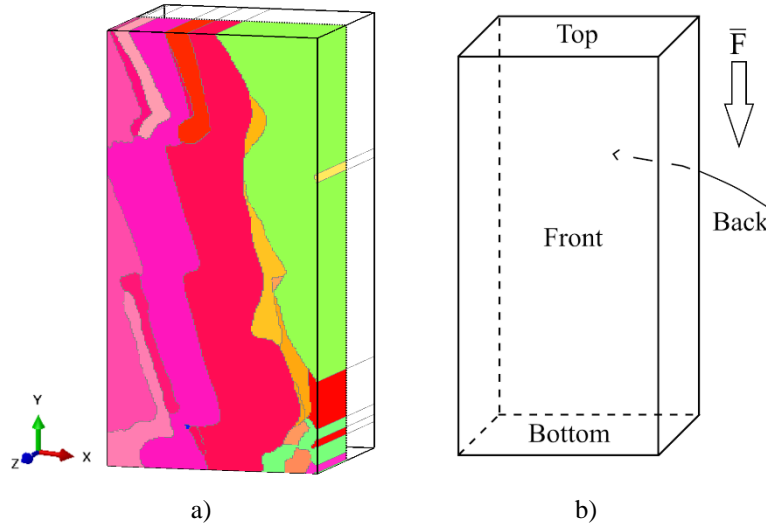


Fig. 3 Experimentally-based grain model (a) and schematics of its loading (b)

An important moment of CPFEM explicit implementation is that constitutive equations are formulated with respect to the local coordinate systems specific for each finite element. In the case at hand, the local frames are associated with the crystal axes which co-rotate with the material under loading. Thus, the generalised Hooke's law is written in the same form for all elements irrespective of their orientations in the global coordinate system:

$$\dot{\sigma}_{ij} = C_{ijkl} (\dot{\epsilon}_{kl} - \dot{\epsilon}_{kl}^p). \quad (1)$$

Here, σ_{ij} denote the stress tensor components, ϵ_{ij} and ϵ_{ij}^p are the total strain and plastic strain tensor components and C_{ijkl} is the fourth-order tensor of elastic moduli. The upper dot stands for time derivative. Three independent elastic modules of a Cu-7.5wt.%Al alloy are $C_{11}=169$ GPa, $C_{12}=122$ GPa, $C_{44}=75$ GPa [30].

The strain rate tensor components $\dot{\epsilon}_{ij}$ are kinematically related to the velocity vector components \dot{u}_i as

$$\dot{\epsilon}_{ij} = (\dot{u}_{i,j} + \dot{u}_{j,i}) / 2. \quad (2)$$

The plastic strain rates are calculated as the summary slip on active slip systems

$$\dot{\epsilon}_{ij}^p = \frac{1}{2} \sum_{\alpha} \dot{\gamma}^{(\alpha)} (s_i^{(\alpha)} n_j^{(\alpha)} + s_j^{(\alpha)} n_i^{(\alpha)}), \quad (3)$$

where $s_i^{(\alpha)}$ and $n_i^{(\alpha)}$ are the components of the slip direction and slip plane normal vectors on the α slip system. An FCC crystal lattice has 12 potentially active $\{111\}\langle 110 \rangle$ slip systems. The slip rate $\dot{\gamma}^{(\alpha)}$ relates to the resolved shear stress $\tau^{(\alpha)}$ acting on the α -th slip system as

$$\dot{\gamma}^{(\alpha)} = \begin{cases} 0, & \text{if } \tau^{(\alpha)} < \tau_{CRSS} \\ \dot{\gamma}_0 \left| \frac{\tau^{(\alpha)}}{\tau_{CRSS}} \right|^v \text{sign}(\tau^{(\alpha)}), & \text{if } \tau^{(\alpha)} = \tau_{CRSS} \end{cases}. \quad (4)$$

The reference slip rate $\dot{\gamma}_0$ linearly depends on the equivalent strain rate $\dot{\epsilon}_{eq}$ calculated specifically for each finite element with the coefficient of 0.9. Thus, the slip rate is naturally higher in the regions of higher strain rate to ensure eliminating the strain rate sensitivity effects [31]. Eq. (4) means that a slip system is activated if the resolved shear stress, $\tau^{(\alpha)} = s_j^{(\alpha)} \sigma_{ij} n_j^{(\alpha)}$ reaches the critical value $\tau_{CRSS}^{(\alpha)}$. The latter is the material property depending on the microstructural features and strengthening mechanisms. A common way to determine the critical resolved shear stress is an approximation of the plastic portion of a stress-strain curve. In this work, $\tau_{CRSS}^{(\alpha)}$ was calculated for each finite element as

$$\tau_{CRSS}^{(\alpha)} = \tau_0 + k \epsilon_{eq}^p \quad (5)$$

where the initial stress value τ_0 assigned the same for all slip systems. The second right-hand term is a linear strain hardening function where ϵ_{eq}^p is the equivalent plastic strain accumulated in the finite element. The values of $\tau_0^{(\alpha)} = 27$ MPa and $k = 270$ MPa were defined to fit the plastic portion of the experimental stress-strain curve, assuming that the critical resolved shear stress is proportionally related to the yield stress through the Schmid factor.

Figure 3b schematically illustrates the load application. The kinematic boundary conditions were put on the specimen top surface to simulate compression along the Y-axis, while the bottom surface displacements along Y were restricted. The back surface was treated as a symmetry plane with respect to Z direction. The other three lateral surfaces were free of external loading.

4. RESULTS AND DISCUSSION

4.1 Surface Pattern and Plastic Strain Distribution

Figure 4 shows an experimental surface image obtained using confocal microscopy after 5% compression. Slip traces are well identified in the surface grains as a series of thin parallel lines inclined to the compression axis. The angle of inclination varies not only from grain to grain but also in various parts of the grains, which indicates the activation of different slip systems there.

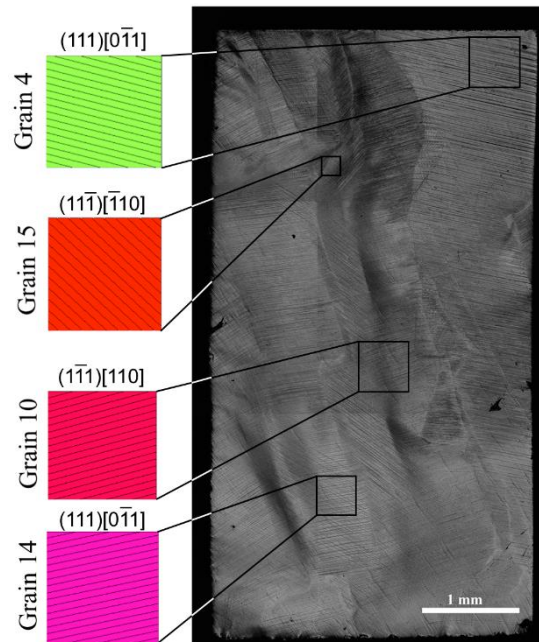


Fig. 4 Experimental surface image of WEB-AM Cu-7.5wt.% Al under 5% compression and analytically predicted slip traces in four selected grains (for the details of the analytical analysis please refer to Section 4.2)

The experimental analysis reveals highly nonuniform plastic deformation developing in sample parts as early as 5% compression. Most regions demonstrate one or two sets of parallel slip lines, with their density varying from region to region. The variation in density is indicative of the amount of accumulated slip – the denser the slip lines, the larger the plastic strain. A prominent example is Grain 10 where several distinct regions with different slip line density and tilt angles are observed. The slip lines tend to change their orientations near grain boundary steps, which indicates that different slip systems are activated. The alignment of slip lines between neighbouring grains is so consistent that it might erroneously suggest slip transfer across grain boundaries. However, recent molecular dynamics simulations [32] showed that slip did not propagate from one grain to another,

but strain gave rise to stress redistribution in the near-boundary region which, in turn, resulted in generating new slip.

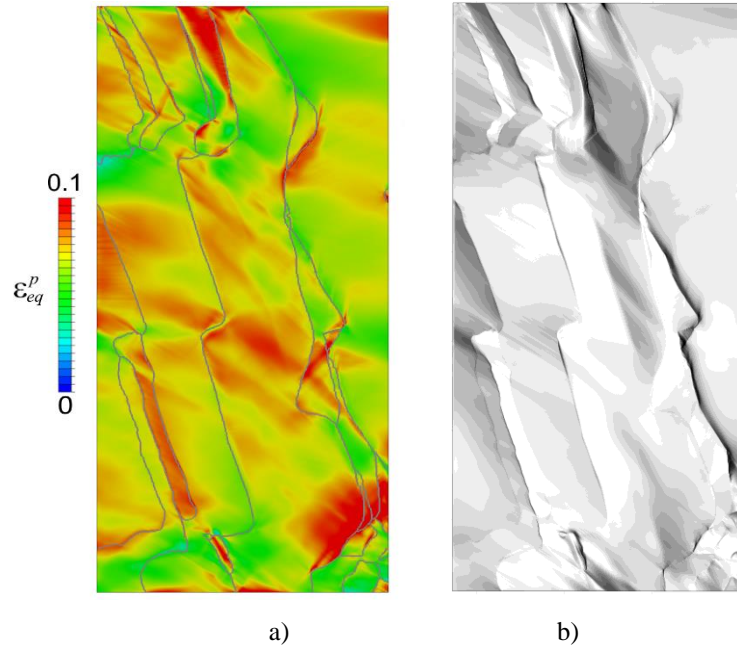


Fig. 5 Equivalent plastic strain field (a) and surface pattern (b) in the oligocrystalline mechanical model under 5% compression

The experimentally based conclusion regarding the plastic strain inhomogeneity is supported by numerical results. Figure 5a, b represents the equivalent plastic strain field and corresponding surface pattern at 5% compression, as obtained in the CPFEM simulation. Despite some simplifications in the computational model, it well captures the key features of the deformation behaviour discovered experimentally. Notably, plastic strains tend to accumulate in the vicinity of stepwise grain boundaries, near boundaries between coarse and fine grains, and in the regions contacting with virtual punches (Fig. 5a). Experimentally, these regions demonstrate a series of more pronounced and dense slip lines, often intersected by another set of slip traces inclined at a different angle (cf. Figs. 4 and 5a).

As plastic deformation develops, the surface of the oligocrystalline model ceases to be flat and the grain boundaries become clearly visible on the surface illuminated by a light source, much like in the experimental image (cf. Figs. 4 and 5b). In general, the model successfully reproduces some experimentally observed features of surface morphology. A case in point is Grain 10 which in both experimental and numerical samples is divided into two parts along its long axis to form a surface fold.

4.2 Analysis of Active Slip Systems

The experimental data, numerical results and analytical estimates were brought together to reveal the peculiarities of slip activation in surface grains under compression. Slip lines, marking where slip planes intersect the surface, provide insight into active slip systems in plastic deformation. In FCC grains, dislocation glide is limited to four $\{111\}$ planes. Therefore, in most cases the active slip plane can be easily determined by the slope of the slip traces once the grain orientation is known. An exceptional case is when equally loaded slip systems may give identical traces of intersection with the surface.

Unambiguous identification of the slip direction is a more sophisticated task that requires the knowledge of slip traces on two adjacent sides of the sample. However, in many cases the slip direction can be analytically determined by comparing Schmid factors in different slip systems calculated from Euler angles. The simplest analytical estimates imply that the Schmid factor for the α -th slip system is calculated with respect to the compression axis

$$F_Y^{(\alpha)} = \cos \varphi \cos \theta, \quad (6)$$

where φ and θ are the angles between the Y-axis and the vectors of slip normal and slip direction, respectively. The slip systems with the highest Schmid factors with respect to the loading axis are most likely to be activated (Table 1).

Table 1 Slip systems with maximal Schmid factors regarding to compression axis

Grain №	Slip system	F_Y	Grain №	Slip system	F_Y
1	(111)[0 $\bar{1}$ 1]	0.4837	13	($\bar{1}$ 11)[0 $\bar{1}$ 1]	0.4937
2	(1 $\bar{1}$ 1)[$\bar{1}$ 01]	0.4651	14	(111)[0 $\bar{1}$ 1]	0.4598
3	(11 $\bar{1}$)[$\bar{1}$ 10]	0.4161	15	(11 $\bar{1}$)[$\bar{1}$ 10]	0.4458
4	(111)[0 $\bar{1}$ 1]	0.4924	16	(1 $\bar{1}$ 1)[110]	0.457
5	(1 $\bar{1}$ 1)[110]	0.4998	17	(1 $\bar{1}$ 1)[110]	0.4552
6	(111)[0 $\bar{1}$ 1]	0.496	18	(1 $\bar{1}$ 1)[$\bar{1}$ 01]	0.3148
7	($\bar{1}$ 11)[0 $\bar{1}$ 1]	0.4924	19	($\bar{1}$ 11)[101]	0.4661
8	(111)[0 $\bar{1}$ 1]	0.4971	20	($\bar{1}$ 11)[101]	0.4867
9	($\bar{1}$ 11)[0 $\bar{1}$ 1]	0.4924	21	($\bar{1}$ 11)[101]	0.4902
10	(1 $\bar{1}$ 1)[110]	0.4586	22	(1 $\bar{1}$ 1)[110]	0.4969
11	($\bar{1}$ 11)[0 $\bar{1}$ 1]	0.4971	23	(111)[0 $\bar{1}$ 1]	0.4604
12	(111)[0 $\bar{1}$ 1]	0.498			

The Schmid factors for 12 $\{111\}\langle 110\rangle$ slip systems were calculated for all 23 grains from the set of Euler angles provided by EBSD. The slip systems with the highest Schmid factors are most likely activated under compression (see Table 1). Indeed, the slip traces which would result from dislocation glide in the analytically predicted slip systems are

detected in all grains. As an example, in Fig. 4 the slip traces analytically predicted and experimentally observed are compared for 4 selected grains. However, additional sets of slip lines, diverging from the analytically anticipated slopes, are also evident in all grains.

The experimental findings align closely with the results of numerical simulations where more than one slip system is activated in most oligocrystal grains. Let us demonstrate this with the example of Grains 4, 10, 14 and 15. Figures 6-9 show the amount of slip accumulated in the four grains at 5% compression, with the slip systems having the largest Schmid factors marked by red frames. The amount of slip in the α -th slip system was calculated for each finite element approximating the grain as

$$\Gamma^{(\alpha)} = \int_t |\dot{\gamma}^p|^{(\alpha)} dt \quad (7)$$

where t is the process time. In two large grains 10 and 14, which extend from the bottom to the top punch, plastic deformation occurs primarily due to dislocation gliding in two slip systems, including those predicted analytically (Figs. 6 and 7). Additionally, one or two slip systems are activated in a few local regions near the grain boundaries to accommodate plastic deformation of adjacent grains. Noticeably, all the slip traces predicted in the simulations are found experimentally in the corresponding grains, as shown in the snippets in Figs. 6-7.

Unlike other grains, Grain 4 has two unconstrained faces so that dislocations have a better ability to glide. In most of this grain, a single slip system is activated, with the exception of a narrow grain boundary region where another slip system becomes active to ensure cooperative plastic deformation with the adjacent grain (Fig. 8). A more complicated scenario is realised in Grain 15 located between Grains 10 and 14 (Fig. 9). Here, four slip systems activating in different parts of the grain make nearly equal contributions to plastic deformation. Notably, the largest contribution is made by a slip system with a non-maximal Schmid factor with respect to the Y-axis. Again, all slip traces predicted numerically are found in Grains 4 and 15 experimentally.

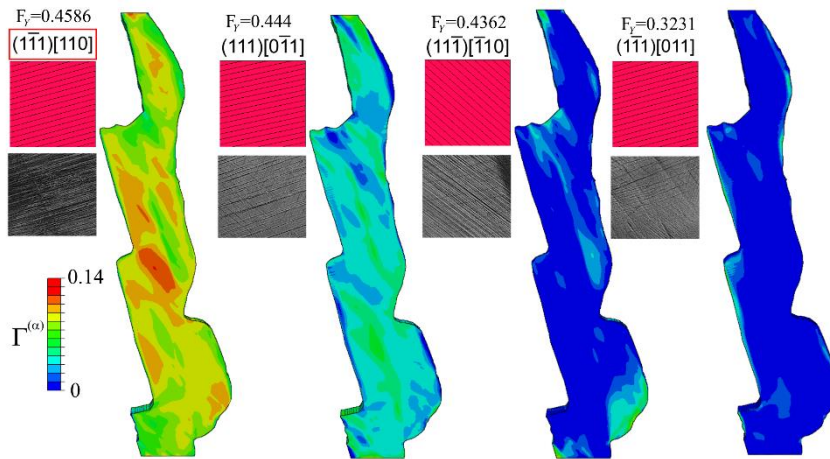


Fig. 6 Amount of slip accumulated in different slip systems in Grain 10 at 5% compression

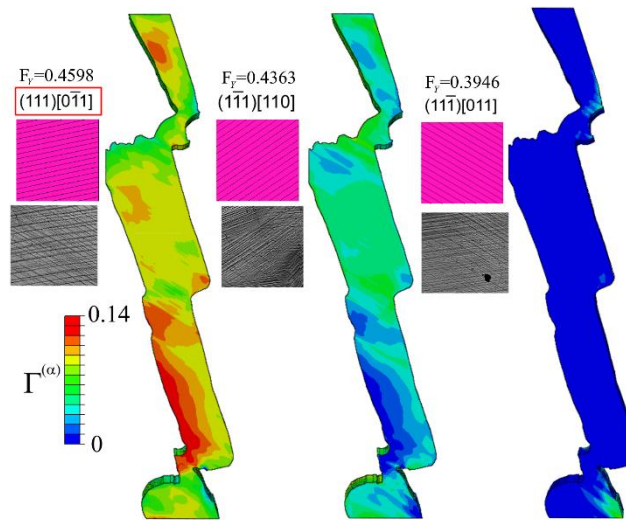


Fig. 7 Amount of slip accumulated in different slip systems in Grain 14 at 5% compression

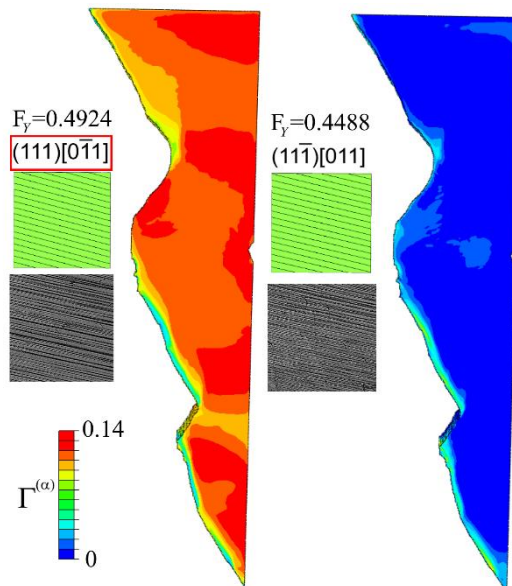


Fig. 8 Amount of slip accumulated in different slip systems in Grain 4 at 5% compression

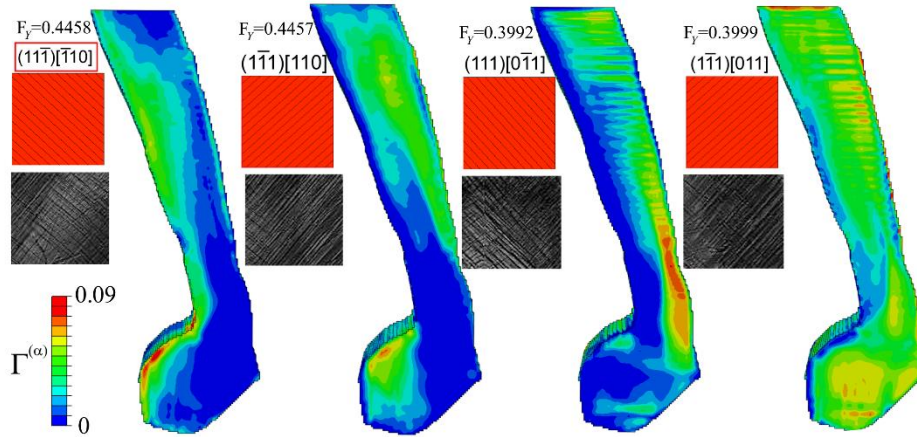


Fig. 9 Amount of slip accumulated in different slip systems in Grain 15 at 5% compression

4.3 Grain-Scale Stress Analysis

To explain why the slip systems with non-maximal Schmid factors become active, let us analyse the stress fields developing in the oligocrystal under compression. The distributions of equivalent stress and stress tensor components acting along and across the loading axis are shown in Fig. 10 for 5% compression. In consistency with the plastic strain field (Fig. 5a), the equivalent (von Mises) stress reveals essential inhomogeneity (Fig. 10a). The higher stresses tend to concentrate near the grain boundaries with large misorientation angles.

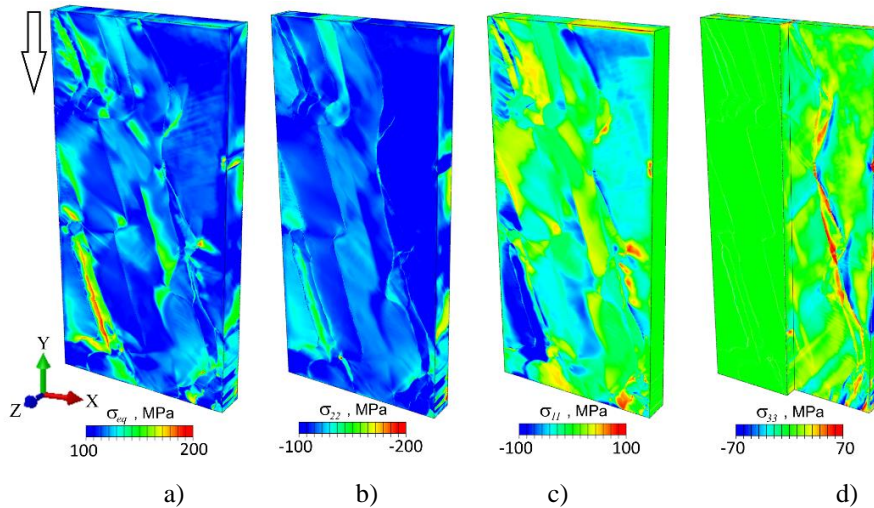


Fig. 10 Equivalent (von Mises) stress (a) and stress tensor components acting along (b) and across the loading axis (c, d) at 5% compression

The analysis of the stress tensor components reveals that the stress state in some local regions deviates from uniaxial. Not surprisingly, the stress σ_{22} acting along the Y-axis takes on negative values all over the computational model, making the largest contribution to the stress state in most grains (Fig. 10b). In some grains, however, the contributions of stresses σ_{11} and σ_{33} acting across the compression axis are comparable to that of σ_{22} , as seen in Fig. 10c-d. The red and blue regions in Fig. 10c exhibit tensile and compressive stresses. The non-zero stresses σ_{11} and σ_{33} may result in activating additional slip systems, disregarded in analytical estimates.

4.4 Strain Rate Dynamics

Numerical simulations provide an exceptional opportunity to trace the development of plastic deformation with high temporal and spatial resolution. In this study, we analysed numerically the strain rate fields evolving during the entire deformation process, which is a challenging task for experimental research. For illustrative purposes, three selected snapshots of the strain rate fields are given in Fig. 11, while the full video is available online (see the supplementary file “StrainRate.mp4”). The local strain rate values in Fig. 11 are normalised to the average strain rate dictated by the velocity of compression. Accordingly, the regions painted with colours located in the colour scale above dark blue deform at strain rates above the average level (the regions with colours between the light blue and red in Fig. 11).

The analysis shows that first plastic strain emerges near the top and bottom corners of the sample, adjacent to the punches (Fig. 11a). In the top corner, slip is initiated in two neighbouring grains 4 and 10 separated by a stepwise high-angle grain boundary. As is discussed above, the slip activation in these grains is dictated by their crystallographic orientations relative to the loading axis. Grain 10 has nearly a Goss orientation with $\langle 110 \rangle \parallel Y$, and Grain 4 is of a Cube orientation with $\langle 100 \rangle \parallel Y$.

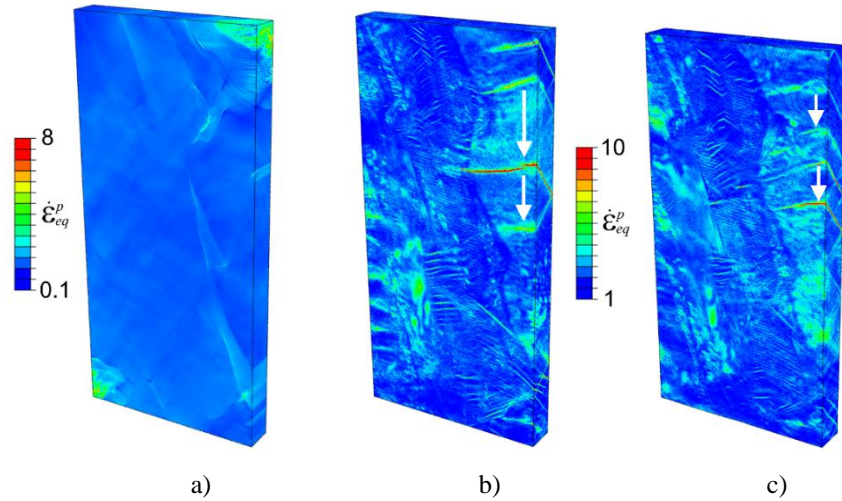


Fig. 11 Snapshots of equivalent strain rate fields in the grain model at a compressive strain of 0.0004 (a), 0.018 (b) and 0.05 (c)

Another decisive factor affecting the scenario of plastic strain evolution in these grains is their position in the sample. An illustrative example is Grain 4 where plastic deformation develops in the form of multiple fronts propagating along the grain body. The plastic strain rate in the narrow zone propagating throughout the grain exceeds the average value several times (red regions in Fig. 11 b, c) and abruptly decreases behind the front. The fronts of localised plastic deformation are periodically generated near the top corner adjacent to the moving punch and subsequently propagate towards the opposite punch at a velocity 1.5-2 times higher than the velocity of compression. This behaviour agrees with the experimental observations of Zuev and Khon [33] and numerical simulations for FCC single crystals [15].

5. CONCLUSION

In this study, we analysed the deformation mechanisms developing in a Cu-7.5 wt.% Al oligocrystal under compression, using a combined experimental and numerical approach. The experimental sample consisting of a few coarse columnar grains was produced by wire-feed electron beam directed energy deposition. Based on the experimental data of EBSD analysis, a crystal plasticity model was built to consider a realistic grain structure. Deformation features of oligocrystal grains under compression were analysed experimentally, numerically and analytically.

The main findings of the study are summarised as follow:

(i) Activation of slip systems: Consistent with theoretical predictions, the slip systems with the highest Schmid factors along the compression axis were activated in all grains. However, up to four additional slip systems were activated in most grains to accommodate their strongly inhomogeneous plastic deformation.

(ii) Complex stress state at grain scale: The study revealed that the stress state at the grain scale considerably deviated from uniaxial. Thus, additional slip systems were at work to balance the non-zero stresses acting across the compression axis.

(iii) Role of grain boundaries in stress concentration: Irregularly shaped grain boundaries are sources of high stress concentration, the relaxation of which also requires the activation of additional slip systems.

(iv) Strain rate dynamics: The numerical analysis of strain rate dynamics with high spatial and temporal resolution showed that plastic deformation in particular grains developed in the form of narrow fronts generated periodically near the moving punch and subsequently propagating towards the opposite side of the sample.

This study has demonstrated that oligocrystal analysis provides valuable insights into the linkage between the intra- and intergrain deformation mechanisms with the overall material behaviour.

Acknowledgement: *The work was performed according to the Government research assignment for ISPMS SB RAS, project FWRW-2021-0002. EBSD data were obtained using an equipment of Tomsk Regional Core Shared Research Facilities Center of National Research Tomsk State University, supported by the Ministry of Science and Higher Education of the Russian Federation through Grant no. 075-15-2021-693 (no. 13.RFC.21.0012).*

REFERENCES

1. Popov, V.L., Heß, M., Willert, E., 2019, *Handbook of Contact Mechanics: Exact Solutions of Axisymmetric Contact Problems*, Springer Berlin Heidelberg, 347 p.
2. Popov, V.L., Li, Q., Willert, E., 2024, *Approximate contact solutions for non-axisymmetric homogeneous and power-law graded elastic bodies: A practical tool for design engineers and tribologists*, *Friction*, 12, pp. 340-355.
3. Willert, E., 2023, *Analytic contact solutions of the Boussinesq and Cattaneo problems for an ellipsoidal power-law indenter*, *Meccanica*, 58(1), pp. 109-117.
4. Maruschak, P., Konovalenko, I., Sorochak, A., 2023, *Methods for evaluating fracture patterns of polycrystalline materials based on the parameter analysis of ductile separation dimples: A review*, *Engineering Failure Analysis*, 153, 107587.
5. Demir, E., Gutierrez-Urrutia, I., 2021, *Investigation of strain hardening near grain boundaries of an aluminum oligocrystal: Experiments and crystal based finite element method*, *International Journal of Plasticity*, 136, 102898.
6. Ueland, S.M., Chen, Y., Schuh, C.A., 2012, *Oligocrystalline shape memory alloys*, 22(10), pp. 2094-2099.
7. Thiruselvam, N.I., Jeyaraam, R., Subramanian, S.J., Sankaran, S., 2021, *Deformation heterogeneity in copper oligocrystals using high-resolution stereo DIC*, *Materialia (Oxf)*, 18, 101164.
8. Thiruselvam, N.I., Jeyaraam, R., Chalapathi, D., 2023, *Post-deformation microstructure analyses of copper oligocrystals using EBSD and crystal plasticity simulation*, *AIP Conf. Proc.*, 2754, 030009.
9. Zhao, Z., Ramesh, M., Raabe, D., Cuitiño, A.M., Radovitzky, R., 2008, *Investigation of three-dimensional aspects of grain-scale plastic surface deformation of an aluminum oligocrystal*, *International Journal of Plasticity*, 24(12), pp. 2278-2297.
10. Lim, H., Carroll, J.D., Battaile, C.C., Buchheit, T.E., Boyce, B.L., Weinberger, C.R., 2014, *Grain-scale experimental validation of crystal plasticity finite element simulations of tantalum oligocrystals*, *International Journal of Plasticity*, 60, pp. 1-18.
11. Lim, H., Carroll, J.D., Battaile, C.C., Boyce, B.L., Weinberger, C.R., 2015, *Quantitative comparison between experimental measurements and cp-fem predictions of plastic deformation in a tantalum oligocrystal*, *International Journal of Mechanical Sciences*, 92, pp. 98-108.
12. Klusemann, B., Svendsen, B., Vehoff, H., 2012, *Investigation of the deformation behavior of Fe-3%Si sheet metal with large grains via crystal plasticity and finite-element modelling*, *Computational Materials Science*, 52(1), pp. 25-32.
13. Raabe, D., Sachtleber, M., Weiland, H., Scheele, G., Zhao, Z., 2003, *Grain-scale micromechanics of polycrystal surfaces during plastic straining*, *Acta Materialia*, 51(6), pp. 1539-1560.
14. Trusov, P. V., Yanz, A.Y., Teplyakova, L.A., 2019, *Direct crystal elastoviscoplasticity model: An application to the study of single crystal deformation*, *Physical Mesomechanics*, 22(4), pp. 275-286.
15. Romanova, V., Balokhonov, R., Zinovieva, O., Lychagin, D., Emelianova, E., Dymnich, E., 2022, *Mechanical aspects of nonhomogeneous deformation of aluminum single crystals under compression along [100] and [110] directions*, *Metals*, 12(3), 397.
16. Ma, X., Zhao, J., Du, W., Zhang, X., Jiang, L., Jiang, Z., 2019, *Quantification of texture-induced ridging in ferritic stainless steels 430 and 430LR during tensile deformation*. *Journal of Materials Research and Technology*, 8, pp. 2041-2051.
17. Korkolis, Y.P., Knysh, P., Sasaki, K., Furushima, T., Knezevic, M., 2023, *Deformation-induced surface roughening of an aluminum-magnesium alloy: Experimental characterization and crystal plasticity modelling*, *Materials*, 16(16), 5601.
18. Batalha, R.L., Pauly, S., Kühn, U., Kosiba, K., Bolfarini, C., Kiminami, C.S., Gargarella, P., 2020, *Oligocrystalline microstructure in an additively manufactured biocompatible Ti-Nb-Zr-Ta alloy*, *Materials Letters*, 262, 127149.
19. Zykova, A.P., Nikolaeva, A. V., Vorontsov, A. V., Chumaevskii, A. V., Nikonov, S.Yu., Moskvichev, E.N., Gurianov, D.A., Savchenko, N.L., Kolubaev, E.A., Tarasov, S.Yu., 2023, *Effect of copper content on grain structure evolution in additively manufactured Ti-6Al-4V alloy*, *Physical Mesomechanics*, 26(2), pp. 107-125.
20. Panin, A. V., Kazachenok, M.S., Krukovsky, K. V., Kazantseva, L.A., Martynov, S.A., 2023, *Comparative analysis of weld microstructure in Ti-6Al-4V samples produced by rolling and wire-feed electron beam additive manufacturing*, *Physical Mesomechanics*, 26(6), pp. 643-655.
21. Kolubaev, E.A., Rubtsov, V.E., Chumaevsky, A. V., Astafurova, E.G., 2022, *Micro-, meso- and macrostructural design of bulk metallic and polymetallic materials by wire-feed electron-beam additive manufacturing*, *Physical Mesomechanics*, 25(6), pp. 479-491.

22. Osipovich, K., Kalashnikov, K., Chumaevskii, A., Gurianov, D., Kalashnikova, T., Vorontsov, A., Zykova, A., Utyaganova, V., Panfilov, A., Nikolaeva, A., Dobrovolskii, A., Rubtsov, V., Kolubaev, E., 2023, *Wire-feed electron beam additive manufacturing: A review*, *Metals*, 13, 279.
23. Wang, H., Lu, Ch., Tieu, K., Liu, Yu., 2021, *A crystal plasticity FE study of macro- and micro-subdivision in aluminium single crystals {001} multi-pass rolled to a high reduction*, *Journal of Materials Science & Technology*, 76, pp. 231-246.
24. Takeuchi, T., 1976, *Work hardening of Cu-10 at%Al alloy single crystals with multiple glide orientations*, *Transactions of the Japan Institute of Metals*, 17(5), pp. 313-321.
25. Schröder, J., Evans, A., Luzin, V., Abreu Faria, G., Degener, S., Polatidis, E., Čapek, J., Kromm, A., Dovzhenko, G., Bruno, G., 2023, *Texture-based residual stress analysis of laser powder bed fused Inconel 718 parts*, *Journal of Applied Crystallography*, 56(4), pp. 1076-1090.
26. Alawadi, A., Abdolvand, H., 2020, *Measurement and modeling of micro residual stresses in zirconium crystals in three dimension*, *Journal of the Mechanics and Physics of Solids*, 135, 103799.
27. Groeber, M.A., Haley, B.K., Uchic, M.D., Dimiduk, D.M., Ghosh, S., 2006, *3D reconstruction and characterization of polycrystalline microstructures using a FIB-SEM system*, *Materials Characterization*, 57(4-5), pp. 259-273.
28. Madej, Ł., Mojżeszko, M., Chrapoński, J., Roskosz, S., Cwajna, J., 2017, *Digital material representation model of porous microstructure based on 3D reconstruction algorithm*, *Archives of Metallurgy and Materials*, 62(2), pp. 563-569.
29. Romanova, V., Balokhonov, R., Emelianova, E., Zinovieva, O., Zinoviev, A., 2019, *Microstructure-based simulations of quasistatic deformation using an explicit dynamic approach*, *Facta Universitatis-Series Mechanical Engineering*, 17(2), 243.
30. Ledbetter, H.M., Naimon, E.R., 1974, *Elastic properties of metals and alloys. II. Copper*, *Journal of Physical and Chemical Reference Data*, 3(4), pp. 897-935.
31. Farooq, H., Cailletaud, G., Forest, S., Ryckelynck, D., 2020, *Crystal plasticity modeling of the cyclic behavior of polycrystalline aggregates under non-symmetric uniaxial loading: Global and local analyses*, *International Journal of Plasticity*, 126, 102619.
32. Nikonov, A.Yu., Lychagin, D. V., Bibko, A.A., Novitskaya, O.S., 2022, *Growth and deformation simulation of aluminum bronze grains produced by electron beam additive manufacturing*, *Metals*, 12(1), 114.
33. Zuev, L.B., Khon, Yu.A., 2022, *Plastic flow as spatiotemporal structure formation. Part I. Qualitative and quantitative patterns*, *Physical Mesomechanics*, 25(2), pp. 103-110.